Nucleation-Governed Reversible Self-Assembly of an Organic Semiconductor at Surfaces: Long-Range Mass Transport Forming Giant Functional Fibers

ARTICLE *in* ADVANCED FUNCTIONAL MATERIALS · DECEMBER 2007

Impact Factor: 11.81 · DOI: 10.1002/adfm.200700549

7 AUTHORS, INCLUDING:

Andrea Liscio
Italian National Research Council
68 PUBLICATIONS **1,225** CITATIONS
SEE PROFILE

Piera Maccagnani
Italian National Research Council
62 PUBLICATIONS **806** CITATIONS
SEE PROFILE

Vincenzo Palermo
Italian National Research Council
130 PUBLICATIONS **2,576** CITATIONS
SEE PROFILE

Paolo Samorì
University of Strasbourg
272 PUBLICATIONS **7,338** CITATIONS
SEE PROFILE

ADVANCED FUNCTIONAL MATERIALS

FULL PAPER

DOI: 10.1002/adfm.200700549

Nucleation-Governed Reversible Self-Assembly of an Organic Semiconductor at Surfaces: Long-Range Mass Transport Forming Giant Functional Fibers**

By *Giovanna De Luca*, *Andrea Liscio*, *Piera Maccagnani*, *Fabian Nolde*, *Vincenzo Palermo*,* *Klaus Müllen*,* and *Paolo Samorì**

The use of solvent-vapor annealing (SVA) to form millimeter-long crystalline fibers, having a sub-micrometer cross section, on various solid substrates is described. Thin films of a perylene-bis(dicarboximide) (PDI) derivative, with branched alkyl chains, prepared from solution exhibit hundreds of nanometer-sized PDI needles. Upon exposure to the vapors of a chosen solvent, tetrahydrofuran (THF), the needles re-organize into long fibers that have a remarkably high aspect ratio, exceeding 10^3. Time- and space-resolved mapping with optical microscopy allows the self-assembly mechanism to be unravelled; the mechanism is found to be a nucleation-governed growth, which complies with an Avrami-type of mechanism. SVA is found to lead to self-assembly featuring i) long-range order (up to the millimeter scale), ii) reversible characteristics, as demonstrated through a series of assembly and disassembly steps, obtained by cycling between THF and $CHCl_3$ as solvents, iii) remarkably high mass transport because the PDI molecular motion is found to occur at least over hundreds of micrometers. Such a detailed understanding of the growth process is fundamental to control the formation of self-assembled architectures with pre-programmed structures and physical properties. The versatility of the SVA approach is proved by its successful application using different substrates and solvents. Kelvin probe force microscopy reveals that the highly regular and thermodynamically stable fibers of PDI obtained by SVA exhibit a greater electron-accepting character than the smaller needles of the drop-cast films. The giant fibers can be grown in situ in the gap between microscopic electrodes supported on SiO_x, paving the way towards the application of SVA in micro- and nanoelectronics.

1. Introduction

Hierarchical self-assembly is a cooperative process that is ubiquitous in nature.[1] Supramolecular chemistry, through the concerted use of different weak forces, enables the formation of nanoscale, thermodynamically stable architectures in solution. Given that the interactions involved are very weak, features like reversibility, response to external stimuli, adaptability, and self-healing are hallmarks of supramolecular structures and materials.[1] While the subtle mechanism governing the self-assembly of supramolecular species in solution has been recently unraveled,[2] the understanding of the self-assembly at surfaces is still very limited: the formation of ordered, self-assembled nanostructures at surfaces is more complicated as it requires the additional control over interfacial interactions.[3] Such an understanding is, however, crucial to achieve full control over the growth across multiple length scales of functional architectures with pre-programmed structure and properties. These architectures can be exploited as active building blocks for application in various fields including (opto)electronics, magnetism, catalysis, and medicine.[1,4]

The performance of organic-based nano- and microelectronic devices strongly depends on the molecular order at the supramolecular level.[5,6] A high intermolecular charge transfer is achieved in crystalline materials combining molecular stacking over large distances and a low density of defects, such as

[*] Dr. V. Palermo, Dr. G. De Luca, Dr. A. Liscio
Istituto per la Sintesi Organica e la Fotoreattività
Consiglio Nazionale delle Ricerche
via Gobetti 101, 40129 Bologna (Italy)
E-mail: palermo@isof.cnr.it
Prof. K. Müllen, F. Nolde
Max-Planck Institute for Polymer Research
Ackermannweg 10, 55124 Mainz (Germany)
E-mail: muellen@mpip-mainz.mpg.de
Prof. P. Samorì
Nanochemistry Laboratory
ISIS – CNRS 7006, Université Louis Pasteur
8, allée Gaspard Monge, 67083 Strasbourg (France)
E-mail: samori@isis-ulp.org
Dr. P. Maccagnani, Prof. P. Samorì
Istituto per la Microelettronica e Microsistemi
Consiglio Nazionale delle Ricerche
via Gobetti 101, 40129 Bologna (Italy)

[**] We thank Matteo Palma for recording the SEM images. This work was supported by the ESF-SONS2-SUPRAMATES project, the Regione Emilia-Romagna PRIITT Nanofaber Net-Lab, and the EU through the projects Marie Curie EST-SUPER (MEST-CT-2004-008128), the RTNs PRAIRIES (MRTN-CT-2006-035810) and THREADMILL (MRTN-CT-2006-036040), and ForceTool (NMP4-CT-2004-013684). Supporting Information is available online from Wiley InterScience or from the author.

impurities or polycrystalline domain boundaries.[7,8] Thus far, the highest performances, in terms of charge mobility, have been obtained on single organic crystals,[9] and values as high as 15 $cm^2 V^{-1} s^{-1}$ were found for rubrene single-crystal transistors.[10] Large macroscopic crystals are typically grown making use of vacuum sublimation and physical vapor deposition,[9] but their electrical wiring is usually a complex process. Moreover, these approaches are not easy to scale up. The use of prepatterned surfaces was successfully employed to achieve control over the vacuum growth and positioning of the crystals.[11] On the other hand, solution growth is much more practical and suitable for technological applications, although it suffers from the reduced size, typically up to the micrometer scale, of the crystals. The morphology obtained from solution casting is ruled by the interplay of intramolecular, intermolecular, and interfacial interactions. A key role is played by physical processes arising from solvent evaporation such as dewetting and contact line pinning.[12–16] Being a kinetically controlled process, the crystalline character of the material can be improved by slowing the solvent evaporation rate by either performing the deposition in a sealed jar,[17] using solvents with low volatility, or reducing the temperature.[16] Post-processing can also be employed to increase the crystalline character of the material. While thermal-annealing treatments are tedious approaches, solvent-vapor annealing (SVA) in an atmosphere saturated with vapors of a solvent in which the organic molecules are soluble appears to be a more tunable and versatile method. Notably, the solvent used for the annealing might also be chosen to have either a poor or a strong interaction with the substrate, potentially offering a way to drive the self-assembly at surfaces towards pre-programmed architectures. In SVA, the solvent molecules adsorb on the substrate, dissolving (partially) the deposited layer, and, thereby, leading to self-healing and ultimately evolution towards thermodynamically stable crystalline morphologies.[18,19] Using this method, it was demonstrated that the electronic properties of the material and the performance of electronic devices can be significantly improved,[20] although the increase in crystalline character was not accompanied by a molecular motion over macroscopic distances but rather by a reorganization on a local (i.e., nanometric) scale. Furthermore, the mechanism governing this process is still unexplored.

Here, we provide for the first time a time-resolved insight across multiple length scales into the process of reversible self-assembly of an organic semiconducting molecule, forming millimeter-long fibers on surfaces upon solvent-vapor annealing treatment. This study reveals that the self-assembly process occurring at a surface can be governed by nucleation. As a model system, we have chosen an n-type semiconductor, *N*,*N*′-bis(1-ethylpropyl)-3,4:9,10-perylene-bis(dicarboximide) (PDI), widely studied for optoelectronics and photovoltaic applications.[21,22] This planar polyaromatic molecule (Fig. 1a and b) can self-associate into highly ordered supramolecular architectures[18,23,24] having a high charge-carrier mobility.[25]

2. Results and Discussion

2.1. Spin-Coated Films of PDI on SiO_x

Upon depositing a PDI solution in tetrahydrofuran (THF) on SiO_x substrates by spin-coating, nanometer-sized needles, having a high aspect ratio, self-assemble at the surfaces (Fig. 1c). Atomic force microscopy (AFM) images reveal that each needle exhibits sharp edges and a uniform thickness, suggesting the crystalline nature of the nano-objects. All the PDI molecules deposited on the surface are assembled into these needles, which display lengths of 190–330 nm, widths of 40–70 nm, and heights of 24–30 nm. However, most of the SiO_x substrate surface remains exposed. Samples spun from chloroform ($CHCl_3$) solutions display a similar morphology consisting of needles having lengths that span 150 to 500 nm, widths ranging from 35 to 70 nm, and heights up to 20 nm (Fig. 1d). These needles, possessing an aspect ratio of about 5, are adsorbed on a discontinuous amorphous ca. 2 nm thick layer, which is most likely formed by a de-wetting process because of non-homogeneous solvent evaporation.[26]

The formation of PDI nanocrystals on the top of the amorphous layer on SiO_x results from the interplay of intramolecular, intermolecular, and interfacial interactions.[16] In particular, $CHCl_3$ is generally regarded as a 'good' solvent for PDI derivatives, as it bears alkyl substituents at the N atoms;[23] hence, solvation will compete with the well-known π–π stacking interactions existing among PDI molecules,[27] leading to the observed self-assembled nanostructures. Besides, given its relatively low dielectric constant, $CHCl_3$ scarcely possesses an affinity for the polar SiO_x surface, favoring the adsorption of the PDI into poorly ordered assemblies, as the amorphous thin de-wetting

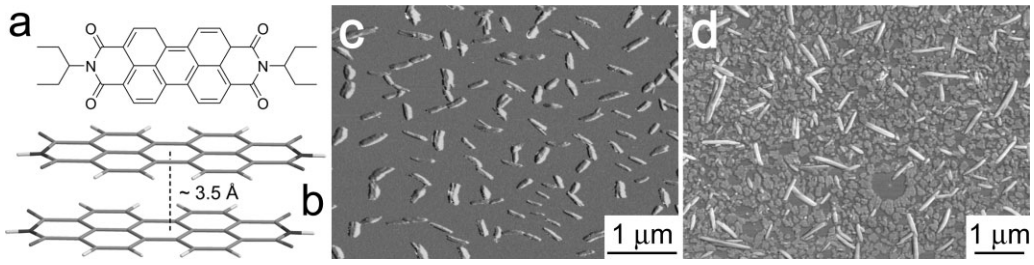

Figure 1. a) Chemical formula of *N*,*N*′-bis(1-ethylpropyl)-3,4:9,10-perylene-bis(dicarboximide) (PDI). b) Most common π–π stacking of PDI molecules in the solid state involving longitudinal and transverse offsets.[22] c,d) Atomic force microscopy (AFM) phase images of PDI nanostructures obtained by spin-coating a 10^{-3} M solution in tetrahydrofuran or $CHCl_3$, respectively, on a SiO_x substrate.

ADVANCED FUNCTIONAL MATERIALS

layer shown in Figure 1d. In contrast, the use of a solvent having a higher dielectric constant, like THF, has a twofold influence as it both favors the self-association of PDI into needles and, in view of its favorable interaction with the polar SiO_x surface, it hinders the kinetically driven (trapped) adsorption of PDI into the amorphous layer on the substrate.

2.2. Solvent-Vapor Annealing of PDI Films on SiO_x

Upon exposure of the nanocrystals obtained from both $CHCl_3$ and THF to an atmosphere saturated with THF vapors, a dramatic change in morphology is observed. AFM, scanning electron microscopy (SEM), and optical microscopy (OM) reveal that all the nanocrystals dissolve (see below) and form macroscopic fibers on the surface, with lengths up to 3 mm. The cross section of the fibers was found to be constant at least over several tens of micrometers, with thicknesses and widths in the sub-micrometer regime, and aspect ratios that exceed 10^3 (Fig. 2a–c). In particular, the width of a single fiber is highly uniform, varying by less than 1 % over a 10 μm length, whereas a finite, yet limited, size dispersion can be noticed by comparing the width of different fibers; however, this is always below 1 μm. A typical example is shown in Figure 2a, where the height of fiber 1 is found to be between 200 and 207 nm and its width amounts to 360 nm, with a maximum variation of 20 nm across a scanned length of about 22 μm.

At the end of the SVA process most of the surface remains uncoated, that is, neat SiO_x remains exposed, as observed by AFM and SEM (Fig. 2a–c). OM investigations reveal that the fibers possess both birefringence (see Supporting Information, Fig. S1) and polarized fluorescence emission, pointing to a high anisotropy of the crystal packing, which is in agreement with literature results.[18,27,28] In particular, the highest emission intensity in the polarized fluorescence microscopy (Fig. 2d and e) images is observed for fibers oriented nearly parallel to the excitation polarization axis, as highlighted by the comparison of a perpendicular fiber-to-polarizer orientation. This evidence indicates that the direction of the 1D molecular packing is nearly aligned with that of the transition dipole moment of a whole perylene assembly. This suggested molecular arrangement is in accordance with the known tendency of conjugated molecules bearing alkyl side groups to pack 'edge-on' on insulating surfaces, forming π–π stacked assemblies.[29]

The structures obtained by SVA are completely different from those formed using other conventional slow methods of deposition from solution. By depositing PDI from a $CHCl_3$ solution on SiO_x via drop-casting in a small sealed container, slow evaporation of the solvent can be attained, and the formation of large and anisotropic needles is observed. The lengths of these objects reach several tens of micrometers, whereas both their widths and heights are typically smaller than 5 μm (Supporting Information, Fig. S2a and c). If compared to the fibers obtained by SVA, the crystals obtained by drop-casting have a much smaller aspect ratio, their width is much more variable, and, more importantly, they show a highly defective structure, with domain boundaries oriented primarily along their main axis (Fig. S2a, c, and d). Interestingly, while the 'classical' crystals obtained by drop-casting are rigid and always linear, the fibers obtained by SVA can bend, although they keep their regular and uniform cross section (e.g., fiber 2 in Fig. 2a), which could be ascribed to their different mechanical properties. When an SVA treatment in THF is performed on drop-cast PDI samples, the larger amount of material present on the surface leads to the formation of a denser network of shorter fibers, often displaying dendritic patterns (Fig S2b).

Kelvin probe force microscopy (KPFM) measurements show that the structures obtained from solution deposition of a PDI solution in $CHCl_3$ on SiO_x and those obtained upon subsequent SVA with THF possess different work functions (WF). These amount to (4.85 ± 0.02) eV and (4.92 ± 0.02) eV, respectively, indicating better electron-accepting character of the highly regular fibers with respect to the structures deposited by conventional solution processing. These values are in good agreement with energy diagrams of PDI reported in the literature.[30] The two WF values suggest that the two assemblies possess different electronic properties, which is most likely caused by their diverse molecular packing at the supramolecular level, as is also independently confirmed by preliminary X-ray diffraction experiments. This result is in line with findings reported by Lahav and co-workers on the formation of different crystal polymorphs from solutions, as controlled by the use of different solvents, taking advantage of the changes that result in the balance between solvent–surface, solute–solvent, and solute–solute interactions.[31]

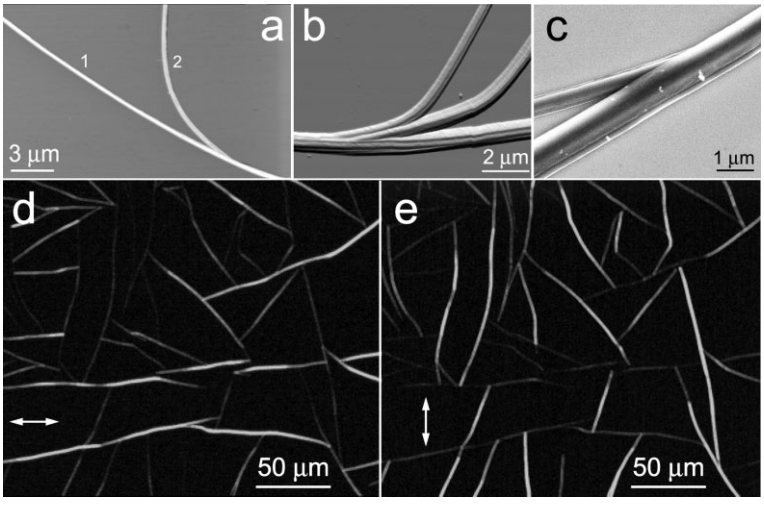

Figure 2. PDI fibers obtained after SVA of samples in THF; the samples had been prepared by depositing a PDI solution in $CHCl_3$ on SiO_x via spin-coating. a) AFM topography, b) AFM topography gradient, and c) SEM images of junctions of the fibers, providing evidence for the homogeneous width and height of the fibers, which do not exhibit structural defects. d,e) Polarized fluorescence microscopy images of the same area of the sample observed with different orientations of the polarizer. White arrows show the direction of the excitation polarization. *Z*-ranges: (a) 345 nm; (b) 3290 nm/nm.

2.3. Time-Resolved Studies of the SVA Process

Given the size of the PDI structures obtained after SVA in THF, and the relatively slow rate of their formation, we investigated the growth of the fibers by monitoring the SVA process in real time using OM. Figure 3a–c displays images recorded in a time frame of 70 min, and the movie (movie S1 in the Supporting Information) shows the entirely dynamic process occurring on a 195 min timescale. AFM and SEM reveal that at the end of the growth process the area outside the fibers exposes neat SiO_x, confirming that all the PDI initially spread on the surface has been phagocytized by the growing fibers. The growth phenomenon is initially characterized by a slow lag phase, in which nuclei are formed. Then, such nuclei rapidly grow, forming millimeter-long fibers. The processing of these images made it possible to follow the evolution of the fiber length versus time. The plot in Figure 3g reveals a sigmoidal profile, suggesting again that the formation of PDI fibers is a nucleation-governed growth process. This is a widespread growth mechanism, which has also been observed for polymerization reactions,[32] phase transformations,[33,34] and for aggregation phenomena involved in important diseases such as Alzheimer's or malaria.[35–37] The modeling of our system behavior using an Avrami equation (see Experimental),[38–40] shows that the fibers' growth can be described as a homogeneous crystallization characterized by continuous nucleation and growth of

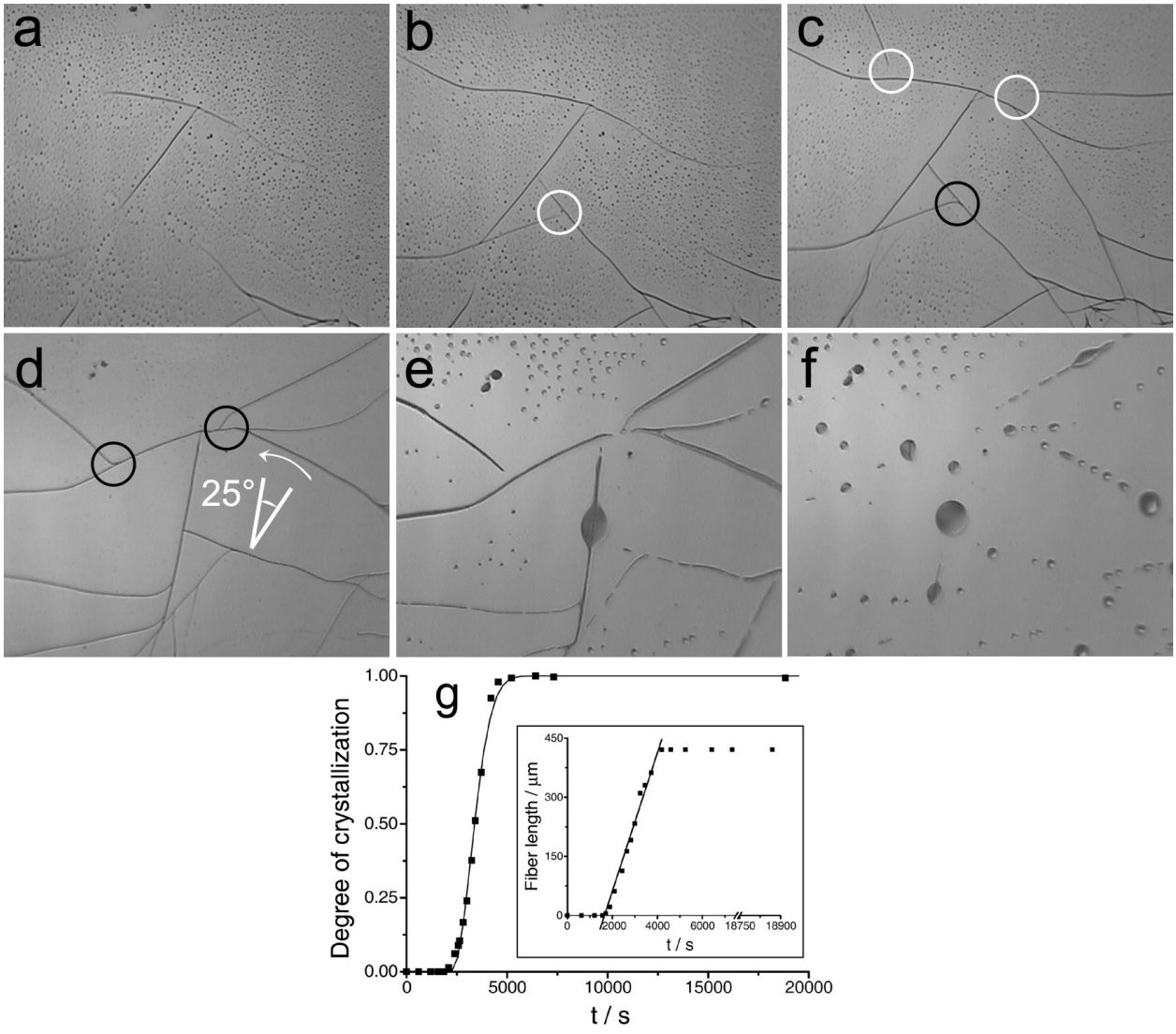

Figure 3. Snapshots from real-time optical microscopy a–c) taken at 44, 57, and 70 min, respectively, during SVA in THF of PDI spin-cast on SiO_x; d–f) The same area, showing fibers dissolution at 0, 60, and 120 min, respectively, during SVA in $CHCl_3$, carried out one day after the fibers were formed (image sizes: 433 µm × 362 µm). The snapshots regard the same zone for both annealing steps, even if a rotation of the sample occurred on replacing the solvent, as indicated in (d). Circles highlight the bending of a fiber when approaching a preformed one, before (white) and after (black) the two fibers collide. The reassembly of the fibers upon a second exposure to THF is shown in Figure S1. g) Typical kinetic profile of the fibers' growth. Dots represent the degree of crystallization (i.e., (fiber length at time t)/(fiber length at $t=\infty$)) versus time, while the solid line is the fit of the Avrami equation to the kinetic data (Avrami exponent $n=2$). Inset: length of a single fiber versus time; the slope of the linear region is (183 ± 7) nm s^{-1}.

ADVANCED FUNCTIONAL MATERIALS

rodlike structures.[38,41] Such an understanding of the growth mechanism of the fibers is of paramount importance for the control of the self-assembly process, and, thus, for the reproducible formation of fibers with well-defined lengths, cross sections, and properties.

Significantly, real-time OM mapping made it possible to highlight the occurrence of bending of a growing fiber before undergoing a collision with another fiber already existing in its growth path (circles in Fig. 3). If the two fibers eventually collide they form an apparently perfect junction (Fig. 2a–c). The observed long-range, repulsive, interfiber interactions cannot be caused by electrostatic or weak (Van der Waals) interactions because the incoming fiber's bending starts at a distance of several micrometers from the already existing one. This effect, which was observed on about 10–20 % of all the samples, might be explained in two ways. In the first explanation, the direction of the growing fiber is dictated by the density of adsorbed PDI molecules at the surface area in question. The area surrounding a pre-existing fiber can be rather uncoated as the fiber has 'consumed' the previously existing material adsorbed at that surface. In this case, the bending is determined by a 'feeding' process, driving the approaching fiber towards regions with a higher adsorbate density (Fig. S3a). In the second scenario, the two fibers expose a liquid-crystalline corona: when two fibers approach one another, their coronae overlap, and the resulting increase in the energy of the system induces bending of the approaching fiber (Fig. S3b). We believe that the latter explanation is rather unlikely since, on the one hand, we have not been able to visually capture the liquid-crystalline corona by AFM and, on the other hand, this PDI derivative does not exhibit liquid-crystalline phases in the bulk at room temperature.

The presence of mesoscopic areas of clean SiO_x at the end of SVA in THF is noteworthy, whereas the starting morphology was that of a thin, uniform layer of PDI: this implies that during annealing, mass transport caused by PDI molecular motion occurred at least over hundreds of micrometers. The measured linear growth rate, averaged over different fibers, amounts to about 180 nm s^{-1} (Fig. 3g, inset). By combining this value with the average volume of PDI adsorbate per square nanometer on the basal plane of the surface before SVA, as determined from AFM measurements (see below), it was possible to roughly estimate the area needed to 'feed' the growth of a PDI fiber. The approximate volume occupied by the nanocrystals on the sample shown in Figure 1d has been calculated using image analysis. As a rough approximation, the density of PDI in the nanocrystals, amorphous layer, and large fibers has been considered to be similar. The amount of material per surface unit has been estimated both by i) summing the volume of all the nanocrystals and the amorphous layer adsorbed on the surface from different AFM measurements, and ii) performing a histogram analysis of the height on various AFM images (after setting the *Z*-value of the SiO_x substrate to zero). Both methods yielded an average value of 2.9 nm^3 of PDI deposited per square nanometer of surface. Thus, it can be roughly calculated that a typical growing fiber, having a cross section of 500 nm × 500 nm, will 'consume' PDI material adsorbed on ca. 16 μm^2 of the substrate basal plane *each second*. This unambiguously confirms the extremely high long-range mass-transport characteristics of such a self-assembly process. Furthermore, the extremely high aspect ratio reached by the PDI fibers, together with the nearly 1D character of the growth of these architectures, points to a much higher reactivity of one crystallographic plane when compared to the others. Such a high directionality is likely to be driven by the π–π stacking interactions between PDI molecules, giving rise to the formation of strongly anisotropic architectures.

2.4. Reversibility of Self-Assembly upon SVA

As expected, SVA in a more polar solvent, such as acetone and methanol, did not give any fiber growth or adsorbate rearrangement, leading to an unchanged morphology. This behavior can be explained in view of the very limited molecule–solvent interaction. On the other hand, in the case of SVA with $CHCl_3$, the surface turned out to rearrange dramatically: chloroform, being a very good solvent for PDI, dissolves the nanostructures adsorbed at the surface and forms drops of PDI during the SVA process (Fig. 3f). Then, upon exposure of these microscopic drops to air, kinetically trapped aggregates, that is, disordered dry grains having sizes of hundreds of micrometers, are formed. Taking advantage of the diverse behavior observed with the two solvents, we exploited the SVA method to obtain reversible disassembly and reassembly, sequentially exposing the PDI samples to different solvents. Upon $CHCl_3$ annealing, the preformed fibers are progressively destroyed, leading to the formation of macroscopic spherical aggregates (Fig. 3d–f). Subsequently, THF is capable of partially dissolving the spherical agglomerates, and, by providing a high molecular mobility on the SiO_x substrate, the macroscopic fibers are formed again (Fig. S4). The reformation of these fibers is much slower, with a growth rate of approximately 20 nm s^{-1} (to be compared with a rate of ca. 180 nm s^{-1} observed for the first fibers). This difference is probably because of a less homogeneous distribution of PDI molecules on the substrate after exposure to $CHCl_3$. By and large, the relatively polar character of THF seems to be a good compromise between the possibility to dissolve the previously deposited PDI molecules and their ability to reassemble. On the other hand $CHCl_3$, while being able to fully dissolve and transport PDI molecules on the surface even over mesoscopic distances, does not favor strong molecule–molecule self-assembly, hindering the formation of large ordered aggregates.

The size of the PDI fibers obtained in this way is similar to those produced by SVA of vacuum-deposited thin layers of tris(8-hydroxyquinoline) aluminum (Alq_3).[42] However, in that case the anisotropic oriented growth was assisted by lithographic patterning of a silicon surface. In contrast, for PDI the growth takes place on a flat surface, and thus the highly anisotropic growth is uniquely governed by intermolecular interactions.

2.5. General Applicability

While strongly depending on the solvent used, the fiber growth takes place on a variety of substrates, including SiO_x, glass, gold, muscovite mica, and highly oriented pyrolytic graphite, pointing to a prime role played by molecule–molecule and molecule–solvent interactions (Fig. 4).[43] Surprisingly, the surface roughness does not hinder the fibers' growth, as proven by the growth on a SiO_x substrate having an exposed patterned Au electrodes.

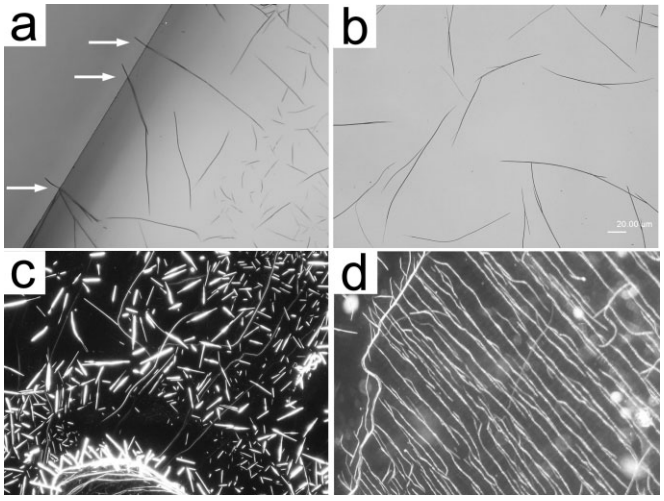

Figure 4. OM images of wires grown on a) SiO_x, b) glass, c) graphite, and d) mica. Albeit the longest fibers have been obtained on flat SiO_x, fiber growth can be performed on metals, insulators, or semiconductors, as proven by their successful growth on gold, mica, glass, and graphite. Interestingly, the drive towards fiber formation is so high that the growth proceeds even over the edges of the substrate, as indicated by arrows in (a). Preliminary results indicate that surface-oriented growth of the fibers can be attained on mica, allowing the fiber's directionality to be controlled; thus, a parallel orientation of the fibers on this substrate is obtained. Also with graphite, the crystal nature of the substrate influences the direction of growth, but in this case shorter needles are formed. This evidence may be ascribed to the apolar character of graphite, which leads to stronger surface–molecule interactions that compete with the self-assembly of the PDI monomers and the growth of long fibers. Image sizes: 370 μm × 280 μm.

The possibility to grow fibers straight over interfaces between different materials opens interesting possibilities to their applications on technologically relevant substrates. Indeed, PDI can be cast from solution over patterned source–drain architectures and then exposed to SVA to grow the fibers in situ (Fig. 5a and b). Current–voltage (*I–V*) measurements performed on samples with or without SVA reveal only in some cases (ca. 20 % of the cases) an improved conductivity for the SVA-treated samples (Fig. 5c). This limited reproducibility is likely to be caused by the low quality of the PDI/gold interface, as also suggested by the diode-like behavior observed on junctions both before and after SVA. The difficulty in obtaining reproducible *I–V* measurements is probably determined by the dependence of the charge-transport performance on the interplay between the material's crystallinity and the quality of the metal/organic interface, which are both modified upon SVA treatment. We will address future studies to the selected modification of only one of these parameters at a time, to get more reliable and reproducible measurements.

3. Conclusions

We have investigated the effect of SVA on the morphology of alkylated PDI thin films, prepared from solution, on various substrates. We have explored in real time the one-dimensional growth of millimeter-long fibers that have a constant cross section of a few hundred nanometers. Such growth was found to comply with an Avrami growth mechanism, that is, it is a nucleation-governed process. Upon exposure to different solvent vapors, the phenomenon revealed a reversible assembly/disassembly behavior. The SVA process is of general applicability, as proved by its successful use with different solvents as well as substrates. This fabrication approach, combining solution casting and vapor annealing, is versatile, cheap, can be scaled up, and does not involve any vacuum processing step; therefore, it is of general interest for application in organic nano- and microelectronics.

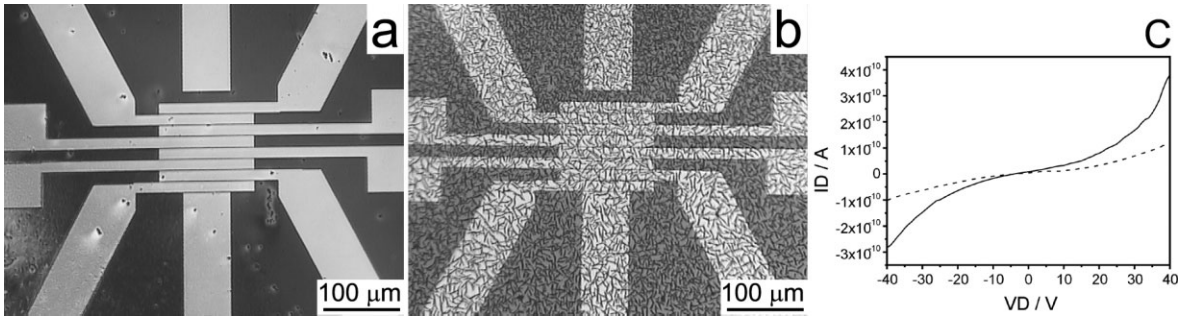

Figure 5. OM images of PDI drop-cast films, supported on a patterned SiO_x surface with exposed gold electrodes, a) before and b) after SVA in THF. Upon fiber formation, the substrate returns to its original, bluish color. c) Current–voltage (*I–V*) characteristics, measured on the samples shown in (a) and (b), are represented with dashed and solid lines, respectively (ID: drain current; VD: drain voltage).

ADVANCED FUNCTIONAL MATERIALS

4. Experimental

All chemicals and solvents used were purchased from Sigma–Aldrich and used as received. All solvents were HPLC grade, whereas hydrogen peroxide (30 % w/w) and ammonium hydroxide (≥ 25 % w/w) solutions were semiconductor grade.

N,N′-Bis(1-ethylpropyl)-3,4:9,10-perylene-bis(dicarboximide) (PDI) was synthesized according to literature methods [44]. After SiO_x/Si samples (ca. 5 μm × 5 μm) were cleaned by using a standard RCA procedure [45], 20 μL drops of a PDI solution (10^{-3} M) in chloroform were either drop-cast or spun (2000 rpm, 60 s) on the substrates in an air environment. The SVA procedure was carried out as described elsewhere [28].

Optical microscopy and polarized fluorescence microscopy images were recorded with a Nikon Eclipse 80i microscope equipped with CFI Plan Fluor Series objectives, a universal epi-fluorescence illuminator (V-2A filter set; excitation filter: 380–420 nm, dichromatic mirror cut-on: 430 nm, barrier filter: 470 nm), rotatable plane polarizer and analyzer, a rotatable mechanical stage, and a DS-2Mv digital camera.

Tapping-mode scanning force microscopy (SFM) [46–48] was employed, recording both the height signal (output of the feedback signal) and the phase signal (phase lag of the tip oscillation with respect to the piezo oscillation). While the first type of image provides a topographical map of the surface, the latter is extremely sensitive to structural heterogeneities on the sample surface, being, therefore, ideal to identify different components in a hybrid film [49,50]. Alongside SFM, Kelvin probe force microscopy (KPFM) [51] was employed in the lift mode. In such a mode, the topography and surface potential (SP) signals are subsequentially recorded. First the surface topography is acquired along a single-line profile. Then a second scan is executed along the same line following the topographic profile at a set lift-height from the sample surface, recording local variations in SP. For more details, see the literature [51]. In brief, KPFM provides a local measure of the SP, which is defined as: $(WF_{tip} - WF_{sample} - \Delta_{pol})/q$, where WF_{tip} and WF_{sample} are the work functions of tip and sample, respectively, Δ_{pol} is the polarization induced by the tip, and q is the magnitude of the elementary charge. In the KPFM experiments performed here, the tip–sample distance amounts to 180 nm; thus, the induced polarization of the surface of the sample can be neglected. In view of this, the measured SP can be assumed as the WF of the sample. For more details, see the literature [52]. The experimental parameters are achieved using the procedure proposed by Jacobs and co-workers [53].

The Multimode IIIA atomic force microscope (Veeco, Santa Barbara, CA, USA) with an Extender Electronics module was run in an air environment at room temperature with scan rates of 1–1.5 Hz/line. Images with scan lengths ranging from 15 μm down to 0.5 μm have been recorded with a resolution of 512 × 512 pixels using the 5 μm scanner and non-contact Pt-coated Si ultra levers (OSCM Veeco) with a spring constant $k < 4$ N m^{-1}. All the measured width values obtained from AFM topographical profiles have been corrected for tip broadening, assuming a 20 nm tip radius, using a previously reported model [54].

Heavily doped silicon single-crystal wafers, coated by a layer of thermally grown SiO_x, either 150 or 750 nm thick, were used as solid substrates for the fabrication of a prototype of a two-terminal device. A 30–40 nm thick layer of Au was successively sputtered: the two coplanar facing Au electrodes were then obtained by a lift-off technique. In this way, electrodes with gaps of 1, 5 and 10 μm have been developed and employed. The *I–V* measurements have been carried out using a computer controlled parametric characterization system.

The growth kinetics of the wires was investigated through real-time optical microscopy experiments, using an annealing chamber equipped with a glass window, which allowed direct observation of the sample during the SVA process. The size (length) of the wires at different times was determined from the optical images by means of SigmaScan Pro 5.0 (Systat Software Inc., Richmond, CA) image analysis software. Data related to global growth phenomena, that is, regarding all the wires formed inside each imaged zone, were transformed from length to crystallization degree by normalizing the values of global length at time t for that at $t = \infty$ (considered as representative of the full crystallization of the sample in that imaged zone) [55].

The system behavior has been modeled using an Avrami equation [38–40,56,57] of the form:

$$Y = 1 - e^{-[k(t-t_i)]^n} \quad (1)$$

where Y is the degree of crystallization, k is the rate constant, t_i corresponds to the induction period, and n is the Avrami exponent. The value of this latter parameter depends both on the dimensionality of the crystal (linear, plate-like, or spherical) and on the nature of nucleation (instantaneous or sporadic), and it is generally an integer number between one and four [38].

Received: May 16, 2007
Revised: June 27, 2007
Published online: November 7, 2007

[1] Special Issue on Supramolecular Chemistry and Self-Assembly, *Science* **2002**, *295*, 2395.
[2] P. Jonkheijm, P. van der Schoot, A. P. H. J. Schenning, E. W. Meijer, *Science* **2006**, *313*, 80.
[3] J. V. Barth, G. Costantini, K. Kern, *Nature* **2005**, *437*, 671.
[4] G. M. Whitesides, M. Boncheva, *Proc. Natl. Acad. Sci. USA* **2002**, *99*, 4769.
[5] A. P. H. J. Schenning, E. W. Meijer, *Chem. Commun.* **2005**, 3245.
[6] F. Cacialli, J. S. Wilson, J. J. Michels, C. Daniel, C. Silva, R. H. Friend, N. Severin, P. Samorì, J. P. Rabe, M. J. O'Connell, P. N. Taylor, H. L. Anderson, *Nat. Mater.* **2002**, *1*, 160.
[7] J. L. Brédas, D. Beljonne, V. Coropceanu, J. Cornil, *Chem. Rev.* **2004**, *104*, 4971.
[8] H. Sirringhaus, P. J. Brown, R. H. Friend, M. M. Nielsen, K. Bechgaard, B. M. W. Langeveld-Voss, A. J. H. Spiering, R. A. J. Janssen, E. W. Meijer, P. Herwig, D. M. de Leeuw, *Nature* **1999**, *401*, 685.
[9] R. W. I. de Boer, M. E. Gershenson, A. F. Morpurgo, V. Podzorov, *Phys. Status Solidi A* **2004**, *201*, 1302.
[10] V. C. Sundar, J. Zaumseil, V. Podzorov, E. Menard, R. L. Willett, T. Someya, M. E. Gershenson, J. A. Rogers, *Science* **2004**, *303*, 1644.
[11] A. L. Briseno, S. C. B. Mannsfeld, M. M. Ling, S. H. Liu, R. J. Tseng, C. Reese, M. E. Roberts, Y. Yang, F. Wudl, Z. N. Bao, *Nature* **2006**, *444*, 913.
[12] R. van Hameren, P. Schon, A. M. van Buul, J. Hoogboom, S. V. Lazarenko, J. W. Gerritsen, H. Engelkamp, P. C. M. Christianen, H. A. Heus, J. C. Maan, T. Rasing, S. Speller, A. E. Rowan, J. Elemans, R. J. M. Nolte, *Science* **2006**, *314*, 1433.
[13] A. M. Higgins, R. A. L. Jones, *Nature* **2000**, *404*, 476.
[14] R. D. Deegan, *Phys. Rev. E* **2000**, *61*, 475.
[15] R. D. Deegan, O. Bakajin, T. F. Dupont, G. Huber, S. R. Nagel, T. A. Witten, *Nature* **1997**, *389*, 827.
[16] V. Palermo, P. Samorì, *Angew. Chem. Int. Ed.* **2007**, *46*, 4428.
[17] D. H. Kim, J. T. Han, Y. D. Park, Y. Jang, J. H. Cho, M. Hwang, K. Cho, *Adv. Mater.* **2006**, *18*, 719.
[18] K. Balakrishnan, A. Datar, R. Oitker, H. Chen, J. M. Zuo, L. Zang, *J. Am. Chem. Soc.* **2005**, *127*, 10 496.
[19] K. C. Dickey, J. E. Anthony, Y. L. Loo, *Adv. Mater.* **2006**, *18*, 1721.
[20] B. A. Gregg, *J. Phys. Chem.* **1996**, *100*, 852.
[21] J. A. A. W. Elemans, R. Van Hameren, R. J. M. Nolte, A. E. Rowan, *Adv. Mater.* **2006**, *18*, 1251.
[22] F. Würthner, *Chem. Commun.* **2004**, 1564.
[23] K. Balakrishnan, A. Datar, T. Naddo, J. Huang, R. Oitker, M. Yen, J. Zhao, L. Zang, *J. Am. Chem. Soc.* **2006**, *128*, 7390.
[24] X. Zhang, Z. Chen, F. Würthner, *J. Am. Chem. Soc.* **2007**, *129*, 4886.
[25] F. Dinelli, R. Capelli, M. A. Loi, M. Murgia, M. Muccini, A. Facchetti, T. J. Marks, *Adv. Mater.* **2006**, *18*, 1416.

[26] E. Rabani, D. R. Reichman, P. L. Geissler, L. E. Brus, *Nature* **2003**, *426*, 271.
[27] A. Datar, K. Balakrishnan, X. M. Yang, X. B. Zuo, J. L. Huang, R. Oitker, M. Yen, J. C. Zhao, D. M. Tiede, L. Zang, *J. Phys. Chem. B* **2006**, *110*, 12 327.
[28] A. Datar, R. Oitker, L. Zang, *Chem. Commun.* **2006**, 1649.
[29] P. Samorì, V. Francke, K. Müllen, J. P. Rabe, *Chem. Eur. J.* **1999**, *5*, 2312.
[30] L. Schmidt-Mende, A. Fechtenkotter, K. Müllen, E. Moons, R. H. Friend, J. D. MacKenzie, *Science* **2001**, *293*, 1119.
[31] I. Weissbuch, V. Y. Torbeev, L. Leiserowitz, M. Lahav, *Angew. Chem. Int. Ed.* **2005**, *44*, 3226.
[32] X. F. Lu, J. N. Hay, *Polymer* **2001**, *42*, 9423.
[33] U. Gasser, E. R. Weeks, A. Schofield, P. N. Pusey, D. A. Weitz, *Science* **2001**, *292*, 258.
[34] S. E. Offerman, N. H. van Dijk, J. Sietsma, S. Grigull, E. M. Lauridsen, L. Margulies, H. F. Poulsen, M. T. Rekveldt, S. van der Zwaag, *Science* **2002**, *298*, 1003.
[35] S. Pagola, P. W. Stephens, D. S. Bohle, A. D. Kosar, S. K. Madsen, *Nature* **2000**, *404*, 307.
[36] R. E. Samuel, E. D. Salmon, R. W. Briehl, *Nature* **1990**, *345*, 833.
[37] Y. S. Kim, T. W. Randolph, F. J. Stevens, J. F. Carpenter, *J. Biol. Chem.* **2002**, *277*, 27 240.
[38] M. Avrami, *J. Chem. Phys.* **1940**, *8*, 212.
[39] S. A. FitzGerald, D. A. Neumann, J. J. Rush, D. P. Bentz, R. A. Livingston, *Chem. Mater.* **1998**, *10*, 397.
[40] J. J. Thomas, H. M. Jennings, *Chem. Mater.* **1999**, *11*, 1907.
[41] A. Yoshioka, K. Tashiro, *Polymer* **2003**, *44*, 6681.
[42] D. J. Mascaro, M. E. Thompson, H. I. Smith, V. Bulovic, *Org. Electron.* **2005**, *6*, 211.
[43] P. Samorì, I. Sikharulidze, V. Francke, K. Müllen, J. P. Rabe, *Nanotechnology* **1999**, *10*, 77.
[44] F. Nolde, J. Q. Qu, C. Kohl, N. G. Pschirer, E. Reuther, K. Müllen, *Chem. Eur. J.* **2005**, *11*, 3959.
[45] W. Kern, D. A. Puotinen, *RCA Rev.* **1970**, *31*, 187.
[46] P. Samorì, *Chem. Soc. Rev.* **2005**, *34*, 551.
[47] S. S. Sheiko, M. Möller, *Chem. Rev.* **2001**, *101*, 4099.
[48] H. Takano, J. R. Kenseth, S.-S. Wong, J. C. O'Brien, M. D. Porter, *Chem. Rev.* **1999**, *99*, 2845.
[49] M. O. Finot, M. T. McDermott, *J. Am. Chem. Soc.* **1997**, *119*, 8564.
[50] P. Leclère, R. Lazzaroni, J. L. Brédas, J. M. Yu, P. Dubois, R. Jérôme, *Langmuir* **1996**, *12*, 4317.
[51] V. Palermo, M. Palma, P. Samorì, *Adv. Mater.* **2006**, *18*, 145.
[52] A. Liscio, V. Palermo, D. Gentilini, F. Nolde, K. Müllen, P. Samorì, *Adv. Funct. Mater.* **2006**, *16*, 1407.
[53] H. O. Jacobs, P. Leuchtmann, O. J. Homan, A. Stemmer, *J. Appl. Phys.* **1998**, *84*, 1168.
[54] P. Samorì, V. Francke, T. Mangel, K. Müllen, J. P. Rabe, *Opt. Mater.* **1998**, *9*, 390.
[55] On extracting kinetic data from OM images, we considered the length as a representative parameter for the fibers' growth instead of the more commonly used volume fraction. As it is not possible to get a direct estimate of the fibers' cross section through OM, in order to use the latter quantity, the fibers' length should be multiplied by a mean cross section value obtained from the AFM measurements. At any rate, this factor would cancel out when dividing the volume at time t by the volume at $t=\infty$. Hence, the two descriptions of the growth processes (length vs. volume) are equivalent in the framework of the proposed kinetic analysis.
[56] M. Avrami, *J. Chem. Phys.* **1939**, *7*, 1103.
[57] M. Avrami, *J. Chem. Phys.* **1941**, *9*, 177.